



# Pore-network model to quantify internal structure and hydraulic characteristics of randomly packed grains with different morphologies

Yunwu Xiong<sup>1,2</sup> · Li Dong<sup>1</sup> · Xiaoxu Long<sup>1</sup> · Minghong Chen<sup>1</sup> · Guanhua Huang<sup>1,2</sup>

Received: 14 October 2019 / Accepted: 29 September 2021

© The Author(s), under exclusive licence to Springer-Verlag GmbH Germany, part of Springer Nature 2021

## Abstract

The flow and transport in porous media are highly dependent on the internal structure and morphology of the pore space. The pore structure is determined by the size and geometrical shape of the solid particles, as well as their distribution and arrangement. In this study, the effect of grains surface morphology on the internal pore structure as well as the flow and transport properties of porous media were quantitatively analyzed using the pore-network approach, with angular quartz sand and round glass beads used as the test substrates. The surface morphology of the grains was visualized through scanning electron microscopy and quantified by Fourier morphological analysis. The pore structure of randomly packed quartz sand and glass beads was visualized using X-ray computed tomography and quantified using the network parameters. The surface morphology of grains with different angularities was distinguished by the shape and angularity parameters calculated from the Fourier representations. The network parameters, including mean coordination numbers, mean pore-body radii, and mean pore-throat radii, of randomly packed angular sand were larger than those of round beads within the same sieving size range. The intrinsic permeability and longitudinal dispersivity in the vertical direction were smaller than those in the horizontal direction, which indicates anisotropic compaction. The intrinsic permeability nonlinearly (power-law) varied with the pore and throat radii of the different extracted networks. The relation between intrinsic permeability and porosity of anisotropic porous media with different grain morphologies followed the Kozeny–Carman equations. Breakthrough curves in the representative elementary volumes of angular sand and round beads exhibited Fickian behavior. The longitudinal dispersivity decreased with an increase in the coordination number regardless of the grain morphology.

**Keywords** Fourier analysis · X-ray computed tomography · Intrinsic permeability · Hydrodynamic dispersion · Grain angularity

## 1 Introduction

Porous media are widely present in diverse scientific and industrial fields at various scales. Various engineering practices, such as exploration of oil, storage and sequestration of CO<sub>2</sub>, and remediation of groundwater contamination, involve flow and transport processes that are highly related

to the pore structure [1, 2]. Similar relevance can be found in construction, where salt damage resulting from efflorescence and sub florescence in the building materials, as well as the drainage capacity and weight of materials, depends on the internal pore structure [3]. In the agricultural field, pore space characteristics affect critical aspects of virtually all soil processes, ranging from the flow and transport of agrochemicals, aeration to biochemical processes [4]. In the chemical and environmental industries, the performance of the filter system is tightly linked to the pore structure of diverse porous media, such as reverse-osmosis desalination. Thus, understanding and quantifying the pore structure and morphology as well as their effects on flow and transport properties, have received great attention in many disciplines.

The pore structure and morphology at different scales affect the flow and transport properties. Variations in pore connectivity and tortuosity at the microscale may result in

✉ Yunwu Xiong  
yxiong@cau.edu.cn

<sup>1</sup> Center for Agricultural Water Research in China, College of Water Resources and Civil Engineering, China Agricultural University, Beijing 100083, People's Republic of China

<sup>2</sup> Chinese-Israeli International Center for Research and Training in Agriculture, China Agricultural University, Beijing 100083, People's Republic of China

complex flow and transport behaviors [5, 6]. Permeability and hydraulic conductivity are the characteristics most affected by the internal structure of the pores. Various laboratory measurements and numerical simulations have been performed to reveal the effect of pore structure on flow properties [7–12]. Narsilio et al. [13] investigated the theoretical links of permeability between the phenomenological Darcy's law and the pore-scale fundamental Navier–Stokes equations for laminar flow ( $Re < 1$ ), and determined that the application of the pore-scale analysis requires characterization of the pore-scale geometry of the porous material. Torskaya et al. [14] found that different grain shapes lead to distinct permeability–porosity compaction trends, and grain surface-to-volume ratio and grain shape are the fundamental physical parameters controlling the fluid flow and distribution. Mahmoodlu et al. [9] simulated the intrinsic permeability of packed sand with different mean grain sizes, and demonstrated that permeability is approximately linear to the mean pore body and throat radii. The intrinsic permeability of coarser sand was found to be much more sensitive to porosity than that of finer sand. Geistlinger et al. [7] demonstrated that pore structure and surface roughness significantly affect the capillary trapping of the non-wetting gas phase during imbibition. The drying kinetics in porous media evidently vary with the coordination number, which characterizes the pore connectivity [15].

The heterogeneity of the pore structure at the microscale increases the complexity and tortuosity resulting in complicated and anomalous transport behaviors [5, 6]. A numerical simulation of diffusion in virtual porous media generated using the Boolean model showed that pore geometry affects the diffusion properties and non-Fickian behavior occurs at the continuum scale [16]. Direct simulations of pore-scale images of different carbonate rocks representing different degrees of pore-scale complexity showed the origin of early breakthrough and long tailing plume behaviors [17, 18]. Transport behavior was presented as Fickian or non-Fickian diffusion significantly affected by pore hierarchy [19]. In addition, pore-scale heterogeneity was found to affect the crystallization and precipitation patterns induced by the evaporation of dissolved salts in porous media, which may result in salt damage to the porous materials, and in parallel alter the structure of the porous material itself. Rad and Shokri [12] found that salt precipitation and dynamics differ with the pore structure packed with grains of different angularities. This salt precipitation was clearly lower than that observed in round media under identical cumulative water loss. Lee and Kurtis [3] demonstrated that the pore structure strongly affected the extent of salt crystallization in cement. Zhang et al. [20] observed that the grain geometry had a more profound effect on the size and configuration of residual nonaqueous-phase liquid contaminants. The residual saturation of the non-aqueous phase liquid tended

to increase as the porous system was composed of more angular or non-spherical grains.

Grain size, geometrical shape, and their arrangement and orientation affect the pore structure of porous media [21]. Different parameters such as sphericity, angularity, and roughness (or eccentricity, roundness, and smoothness) have been widely used to describe the grain shape [22]. To quantitatively express the grain angularity, a shape index called the volume ratio to an ellipsoid, was proposed by Katagiri et al. [23], which can account for the difference in grain angularity. Alternatively, the Fourier technique has been proposed, which is favored in the analysis of the roughness and textural features of granular particles. The Fourier morphological analysis does not suffer from the re-entrant angle problem, thus, it is widely used to describe individual particles because of its flexibility and ease of use [24]. Laubie et al. [25] and Wang et al. [26] proposed a disorder index to characterize the random arrangement of particles.

However, an accurate measurement and characterization of pore structures at different scales remains challenging. Imaging techniques, such as X-ray computed tomography (CT) and magnetic resonance imaging, provide a nondestructive visualization of the internal structure of porous media [27–29]. CT can provide non-invasive three-dimensional (3D) images by mapping X-ray absorption through porous media. A series of digital image processing is required to reduce the noise by filtering, enhance the phase contrast, and segment the grayscale data into two- or multi-class phases [30, 31].

Quantification of the pore structure requires characterization of the topological, geometrical, and morphological configurations of the pore space. A wide variety of methods are available for quantifying 3D pore structures, such as fractal theory, integral geometry, chord-length distribution, pore-level property correlator, Boolean random sets, and cellular automata [32–34]. The pore network is physically characterized by the size distribution, shapes, and spatial arrangement of pores, from which further properties can be derived including connectivity and surface area [35, 36]. The pore structure is quantified in terms of pore body distribution, pore throat distribution, total throat length, and coordination number. The coordination number denotes the number of neighboring pores to which a certain pore is connected, which characterizes the pore connectivity [37]. The concepts such as skeletonization, medial axis, and thinning are widely used to extract pore network [38, 39]. Recently, flow and transport processes have been directly simulated in a pore structure that is mapped using an imaging technique. Direct models include moving particle semi-implicit [40], smoothed particle hydrodynamics [41], lattice Boltzmann [42], and finite element [43]. These models are computationally expensive and may not be suitable for multiphase flow at irregular fluid–solid boundaries and fluid–fluid interfaces

[44]. In contrast, the pore-network model can be used to calculate the permeability and water retention curves under certain initial and boundary conditions [45–47]. The power of the pore-network approach also lies in the fact that it requires less computational capacity. The study aims to quantify the influence of grain morphology on the internal pore structure and the flow and transport properties of porous media. For this purpose, diverse porous structures are generated through the random packing of grains with different morphologies. The pore structures are visualized using X-ray CT, and pore networks are extracted and analyzed from the CT images. The flow and transport properties of different pore structures are simulated based on the extracted pore networks.

## 2 Material and methods

### 2.1 Porous column packing

Quartz sand and glass beads were used as the test substrates to analyze the effects of grain morphology on the pore structure and hydraulic properties. Quartz sand and glass beads were passed through sieves with 14, 16, 18, and 30 meshes, and two groups of grains were arbitrarily selected: fine grains with size of 0.6–0.9 mm and coarse grains with size of 1.0–1.4 mm. The other two groups were prepared by mixing quartz sand and glass beads of 0.6–0.9 mm and 1.0–1.4 mm sizes (1:1 ratio), respectively. The quartz sand and glass beads were packed into Plexiglas columns with an inner diameter of 30 mm and a height of 100 mm. Oven-dried quartz sand and glass beads were continuously poured into the column and compacted using a specific metal hammer to improve the settling. The packing bulk density of the quartz sand and glass beads was  $1.50 \pm 0.6 \text{ g cm}^{-3}$  and their packing height was 95 mm.

### 2.2 Characterization of particle surface morphology

The surface morphology of the particles was measured using scanning electron microscopy (SEM). The SEM images are gray and can reflect the relative surface roughness according to the principle of electronic imaging. The grains were adhered onto a metal sample plate with double-sided adhesive tape and then coated with a carbon film to enhance conductivity. Surface morphology and element distribution images were acquired using a Merlin field-emission scanning electron microscope (Fig. 1). More than 100 grains were scanned for each group.

The surface morphological properties of the single grains (including the grain size, shape, and surface roughness) were characterized using Fourier analysis [24]. An image of an individual particle was cropped from the SEM image, and the edge of each particle was detected using the Canny edge

detector. The center of gravity of each particle was calculated and set as the origin of the polar coordinate system (Fig. 2). Thus, a particle profile can be characterized as a Fourier series, as follows:

$$R(\theta) = R_0 + \sum_{m=1}^M [a_m \cos(m\omega\theta) + b_m \sin(m\omega\theta)] \tag{1}$$

where  $R(\theta)$  is the radius at angle  $\theta$ ,  $M$  is the total number of harmonics,  $R_0$  is the average radius,  $a_m$  and  $b_m$  are the Fourier coefficients, and  $m$  is the harmonic number. The average radius of the particle profile is expressed as

$$R_0 = \frac{1}{2\pi} \int_0^{2\pi} R(\theta) d\theta \tag{2}$$

In addition, the cross-sectional area of the particle is,  $A_0$ , can be expressed as

$$A_0 = \int_0^{2\pi} \frac{1}{2} R^2(\theta) d\theta = \pi \left[ R_0^2 + \frac{1}{2} \sum_{m=1}^{\infty} (a_m^2 + b_m^2) \right] \tag{3}$$

An equivalent radius  $R_{eq}$  yielding the same cross-sectional area can be defined as

$$R_{eq} = \left[ R_0^2 + \frac{1}{2} \sum_{m=1}^{\infty} (a_m^2 + b_m^2) \right]^{\frac{1}{2}} \tag{4}$$

In the Fourier analysis, the shape parameter ( $\alpha_s$ ) and angularity parameter ( $\alpha_r$ ) are used to describe the shape and angularity of the particle, respectively (Fig. 2). The expressions for  $\alpha_s$  and  $\alpha_r$  are

$$\alpha_s = \frac{1}{2} \sum_{m=1}^{N_1} \left[ \left( \frac{a_m}{R_0} \right)^2 + \left( \frac{b_m}{R_0} \right)^2 \right] \tag{5}$$

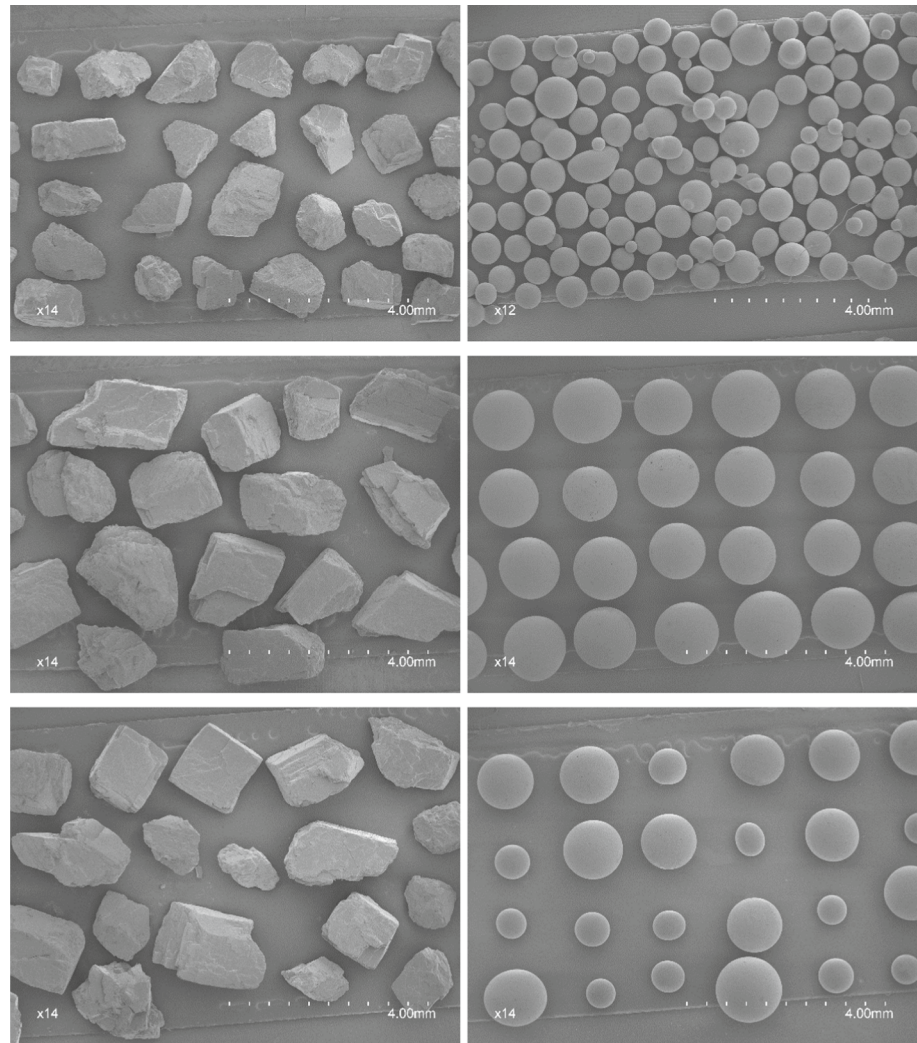
$$\alpha_r = \frac{1}{2} \sum_{m=N_1+1}^{N_2} \left[ \left( \frac{a_m}{R_0} \right)^2 + \left( \frac{b_m}{R_0} \right)^2 \right] \tag{6}$$

where  $N_1$  and  $N_2$  represent the threshold frequencies separating the shape and angularity features, respectively. According to Wang et al. [48],  $N_1=4$  and  $N_2=25$  are the thresholds for quantifying the shape and angularity features.

### 2.3 Visualization of pore structure using CT scan

The pore structure of the packed quartz sand and glass beads was visualized using a cone-beam CT system (YXLON CT Modular, Comet Group). The porous column was mounted onto a rotation stage and scanned at 180 kV and 0.25 mA exposures. An aluminum filter was placed between the X-ray

**Fig. 1** SEM images of angular quartz sand and round glass beads passed through different sieves: (Up) 0.6–0.9 mm, (Middle) 1.0–1.4 mm, and (Bottom) 0.6–1.4 mm which is mixture of 0.6–0.9 and 1.0–1.4 mm with equal ratio of mass



source and the column to minimize the beam-hardening artifacts and highlight the differences in each phase. The column was rotated at intervals of  $0.25^\circ$  and 1440 projections were obtained, which were reconstructed to 3D imagery with a voxel size of  $50\ \mu\text{m}$ .

The CT images were de-noised using a median filter after comparing several filtering algorithms. The calculated median filter replaced the gray value of the considered pixel with the median value of its surrounding voxels (or window) [31]. The appropriate window size and filtering performance were determined using the normalized mean-square error and peak signal-to-noise ratio.

The pore and solid grains were segmented using Otsu's thresholding algorithm, which is a variation of nonparametric and unsupervised iterative global thresholding [49]. The basic concept of Otsu's method is to determine a single optimal threshold in the histogram, where the sum of the foreground and background spreads is at its minimum. The algorithm involves iteration through all possible threshold values and calculation of the optimal threshold

for segmentation (i.e., the pixel that either falls in the foreground or background). The pixels whose intensity values exceeded the threshold value were classified as solid particles, and the remaining pixels were pores. The gray-level histogram was normalized and regarded as a probability distribution.

Analysis of 3D images requires high computational capacity; thus, the structure of a representative elementary volume (REV) rather than a full tomography image was analyzed for each column [50, 51]. An appropriate size of the REV was determined using the conventional point-centered cube geometry approach. The starting voxels were randomly and uniformly located in each column, thus, the sub-volumes slightly overlapped at different locations. The porosity was selected as an indicator for the determination of REV. Two criteria were selected to determine the REV size: the relative gradient error ( $\epsilon_g$ ) and relative standard deviation ( $\sigma_r$ ). For the relative gradient error approach, the REV was selected as the minimum window length scale at which the absolute value of the relative gradient errors was in the range of the

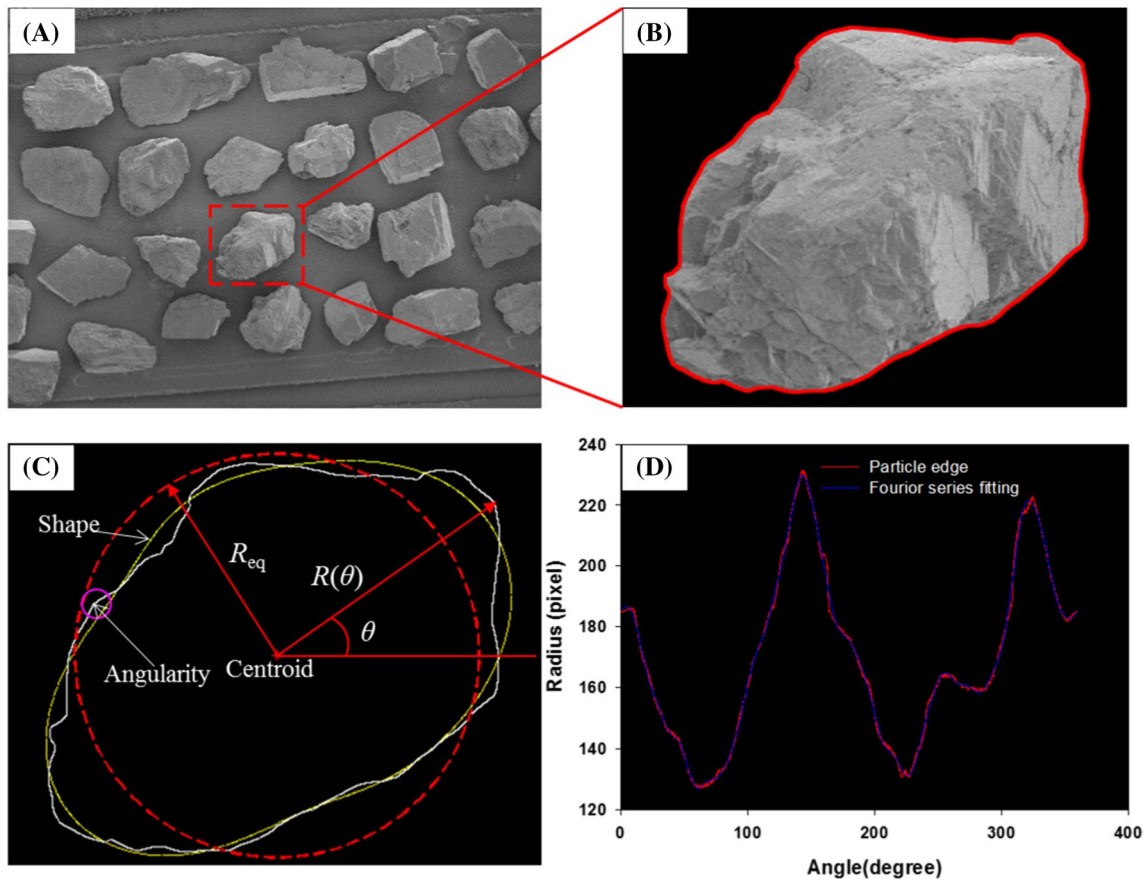


**Fig. 2** Characterization of particles surface morphology using Fourier series: **a** SEM image of 1.0–1.4 mm quartz sand, **b** boundary trace of the sand particle using the Canny edge detector, **c** equivalent

radius of sand particle, and **d** comparison of the edge of sand particle and Fourier series

measured system error. The relative gradient error of the porosity can be calculated as [50]

$$\epsilon_g = \left| \frac{\phi^{i+1} - \phi^{i-1}}{\phi^{i+1} + \phi^{i-1}} \right| \frac{1}{\delta} \tag{7}$$

where  $i$  is the window increment number,  $\phi$  is the porosity of the REV, and  $\delta$  is the magnitude of the increment in the length scale. The relative standard deviation refers to the consideration of the relative standard deviation values for different repetitions during the enlargement processes. The relative gradient error ( $\epsilon_g$ ) and relative standard deviation ( $\sigma_r$ ) had arbitrary determination values. For example, the relative gradient error was set as 0.2 by Costanza-Robinson et al. [50] and the relative standard deviation was set as 0.05 by Xiong et al. [52]. In the present study, for simplification and convenience, all REVs were chosen with a size of  $200 \times 200 \times 200$  voxels, which represents a physical size of  $10 \times 10 \times 10 \text{ mm}^3$  CT image data. This size is still in the plateau stage for all quartz sand and glass bead columns [53]. Five REV-size sub-volumes were used to analyze the

internal pore structure and hydraulic properties of each column. The center points of the subvolumes were uniformly distributed along the vertical axis of each column.

### 2.4 Pore-network extraction

Pore networks of porous media packed with different grain morphologies were extracted using the maximal ball algorithm [54], whose basic concept is to determine the largest inscribed spheres centered on each image voxel that just touches the grain or boundary. Those spheres, which are included in other spheres, are removed, and the rest are called maximal balls [37, 55]. The algorithm of the maximal ball distinguishes between the pore bodies and pore throats, and establishes their respective volumes and connectivity. Dong and Blunt [54] developed a two-step searching algorithm to address the problem of high coordination numbers and improve the computational efficiency of the maximal ball approach. Using this algorithm, a clustering process was developed to define pores and throats by affiliating the maximal balls into family trees according to their size and

rank. The general processes of the two-step search maximal ball extraction algorithm include building maximal balls, clustering the maximal balls, segmenting the pore space and calculating the parameters. A two-step search algorithm following Dong and Blunt [54] was used in the present study.

## 2.5 Flow and transport property simulation

Permeability is a property of porous media that indicates the ability of fluids to flow through. Intrinsic permeability is a function of the internal pore structure. The permeability of porous media with different angularities was simulated based on the extracted network topology. Four assumptions were considered in the network simulation: (1) the connections between pores were considered as round pipes, (2) the pressure drop in a pore was neglected, (3) perfect mixing occurred in the pores, and (4) the flow in the throat was laminar flow. Therefore, the flow rate in an individual throat can be expressed by the Hagen–Poiseuille equation

$$q_{ij} = \frac{\pi R_{ij}^4 (P_i - P_j)}{8\mu L_{ij}} \quad (8)$$

where  $q_{ij}$  is the flow rate between the  $i^{\text{th}}$  and  $j^{\text{th}}$  pores,  $P_i$  and  $P_j$  are the water pressures at pores  $i$  and  $j$  connected by a throat,  $R_{ij}$  is the radius of the pore throat between the  $i^{\text{th}}$  and  $j^{\text{th}}$  pores,  $L_{ij}$  is the length of the pore throat, and  $\mu$  is the fluid viscosity. The mass conservation at each pore is used to solve the pressure distribution and flow rate in the network throats.

$$\sum_{j=p_1}^{p_n} q_{ij} = 0 \quad (9)$$

where  $p_1, \dots, p_n$  are the pores connected to the  $i^{\text{th}}$  pore. The inlet and outlet pressures were assumed to be constant, and the flow rate at the outlet interface was summarized as the total flow rate through the network. The intrinsic permeability was calculated using Darcy's law:

$$k = \frac{\mu QL}{A(P_{in} - P_{out})} \quad (10)$$

where  $L$  is the length,  $A$  is the cross-sectional area of the network,  $Q$  is the total flow rate through the network in the considered direction, and  $P_{in}$  and  $P_{out}$  are the pressures imposed on the inlet and outlet sides of the network, respectively.

The primary drainage water retention curve was calculated using the network. The extracted pore network was first saturated with water, and then, air invasion was enforced at the throats located on the inlet boundary. Quasi-static air invasion controlled by capillarity was assumed so that the viscosity effect could be ignored. The pore throat at the top face was connected to the air

reservoir, and the throats on the bottom face were connected to a water reservoir. The pore throats on the other faces did not flow across the boundaries. Air started to invade the largest throat at the inlet boundary, and with an increase in pressure, smaller throats were invaded, resulting in water desaturation. The water retention curve was obtained through the invasion and desaturation processes until equilibrium. The primary drainage curve was simulated using an invasion percolation algorithm [56], which is well-adapted to study the flow process in which the viscosity effect is negligible and capillarity dominates the flow behavior. The main steps are as follows:

- (1) Identifying the air–water interface of the largest pore-throat under the current water distribution state, and calculating the air-entry pressure using the Young–Laplace equation

$$P_e = \frac{2\gamma \cos \beta}{R_m} \quad (11)$$

where  $P_e$  is the air-entry pressure,  $\gamma$  is the interfacial tension,  $\beta$  is the contact angle, and  $R_m$  is the maximum radius of the pore throat.

- (2) Calculating the difference in pressure between the air and water reservoirs

$$P_c = P_{air} - P_{water} \quad (12)$$

where  $P_c$  is the capillary pressure,  $P_{air}$  is the pressure induced in the air reservoir at the top boundary, and  $P_{water}$  is the pressure induced in the water reservoir at the bottom boundary. For a pore throat, as the capillary pressure exceeds the air-entry pressure, air will invade the pore throat filled with water. If the air-entry pressure is high enough to invade the throat, the pore body connected to this throat will be invaded as well; thus, the pore throat is a dominate element that controls the water distribution at each pressure increment.

- (3) Updating water distribution in the pore-network and boundary condition at the top face, and repeating the calculation processes under a new pressure status. The primary drainage curve of porous media with different angularities was simulated using the OpenPNM package [57].

The simulated drainage curve was fitted using the van Genuchten model [58]:

$$\theta_w = \frac{\theta_s - \theta_r}{[1 + |\alpha h|^n]^{1-\frac{1}{n}}} + \theta_r \quad (13)$$

where  $\theta_w$  is the volumetric water content;  $\theta_s$  is the saturated water content;  $\theta_r$  is the residual water content which is

approximately equal to zero;  $\alpha$  and  $n$  are the shape parameters; and  $h$  is the pressure head.

Hydrodynamic dispersion is an essential mechanism for characterizing solute transport in porous media. Hydrodynamic dispersion combines molecular diffuse driving by solute concentration and mechanical dispersion caused by local variations in the velocity field [59]. Dispersion occurs either in the same direction as that of the net flow (longitudinal dispersion) or perpendicular to the flow (transverse dispersion). Longitudinal dispersion can be expressed as

$$\frac{\partial C}{\partial t} - D_L \cdot \nabla^2 C + v \cdot \frac{\partial C}{\partial z} = 0 \tag{14}$$

where  $C$  is the solute concentration,  $D_L$  is the longitudinal dispersion coefficient, and  $v$  is the average flow velocity in the porous media. The longitudinal dispersion coefficient can be expressed as

$$D_L = \alpha_L v + D_{eff}$$

where  $\alpha_L$  is the coefficient of longitudinal dispersivity and  $D_{eff}$  is the effective diffusion coefficient of the solute. The average flow velocity can be calculated as follow:

$$v = \frac{Q}{A\phi} \tag{16}$$

In the pore network, pressure was imposed in different directions to simulate steady flow and compute the pressure distribution of the pore body (Fig. 3a). A solution with a

concentration of  $1 \text{ mol m}^{-3}$  conservative solute was injected from the inlet, and the concentration at the outlet was zero. The transient concentration distribution of the solute at all pores and throats was calculated (Fig. 3b). Thus, breakthrough curves were obtained by computing the temporal solution concentration at  $z=L/2$  of the pore networks. The longitudinal dispersion coefficient can be calculated as [46]

$$D_L = \frac{z^2}{8} \left[ \frac{1 - t_{0.16}/t_{0.5}}{\sqrt{t_{0.16}}} - \frac{1 - t_{0.84}/t_{0.5}}{\sqrt{t_{0.84}}} \right]^2 \tag{17}$$

where  $t_{0.16}$ ,  $t_{0.5}$ , and  $t_{0.84}$  indicate the times which the solution concentrations are 0.16, 0.5, and 0.84  $\text{mol m}^{-3}$ , respectively. Breakthrough curves were simulated under four different pressure gradients (i.e., 1, 10, 100, and 1000 kPa) which correspond to four different flow velocities (Fig. 4a). Finally, the coefficient of longitudinal dispersivity ( $\alpha_L$ ) was obtained by calculating the slope of the longitudinal dispersion coefficient versus the average flow velocity (Fig. 4b).

### 3 Results and discussion

#### 3.1 Characterization of grain morphology

The surface morphology of an individual grain was analyzed and quantified using Fourier representations. The parameters used to characterize the particle projection

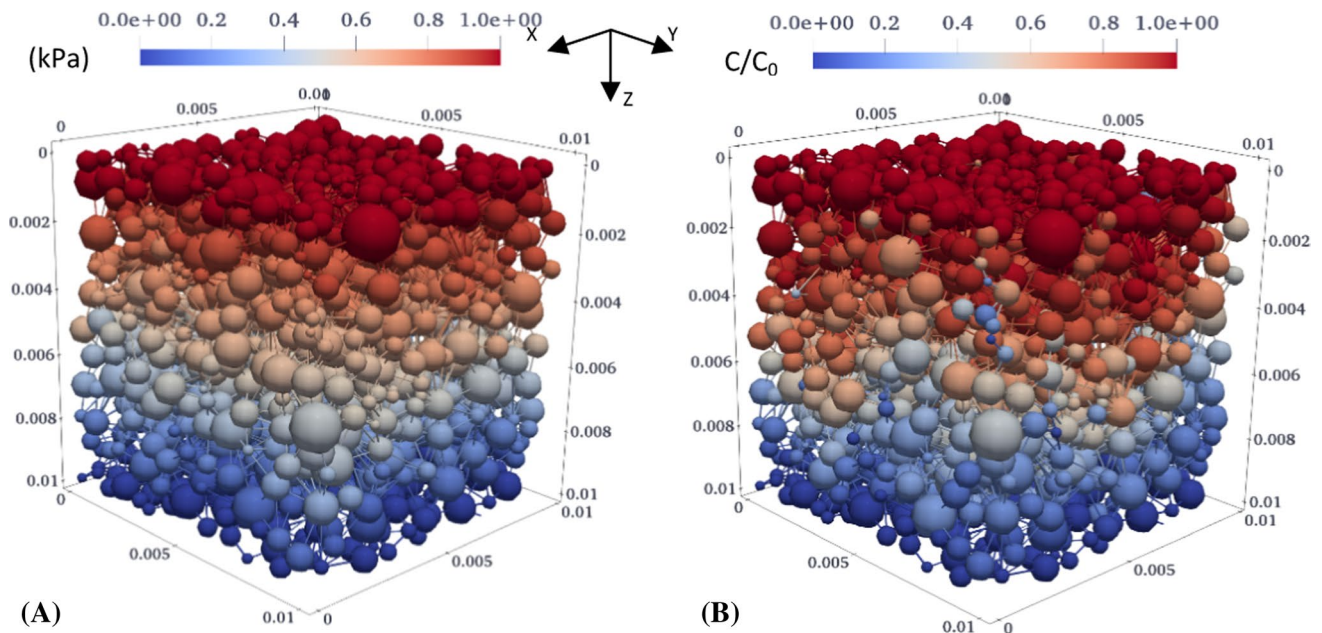


**Fig. 3** Simulation of permeability and dispersivity in vertical direction using the extracted pore network of glass beads (0.6–0.9 mm): **a** pressure distribution in pores, and **b** solute concentration distribution in pores

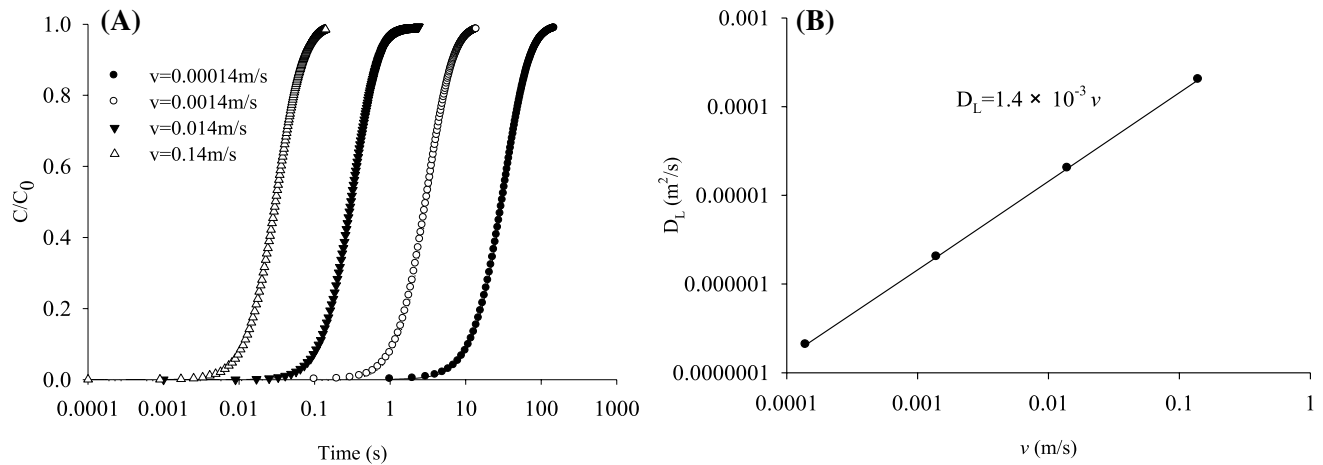


**Fig. 4** Simulation of longitudinal dispersivity of glass beads with size of 1.0–1.4 mm: **a** Breakthrough curves of pore network under different velocities, and **b** linear relation between hydrodynamic dispersion and flow velocity

included the equivalent diameter, shape and angularity parameters (Table 1). The equivalent sizes of the round beads obtained from the Fourier analysis were close to the mean values of the sieving size (0.75, 1.20 and 1.00 mm, respectively). However, the equivalent sizes of the angular sand were slightly larger than the corresponding mean sieving sizes. The mean values of the shape parameter ( $\alpha_s$ ) and angularity parameter ( $\alpha_r$ ) were used to quantify the morphological features. The shape parameters with large magnitude and low frequency in the Fourier representation were related to the boundary shape, and the angularity parameters with small magnitude and high frequency were related to the angular character superimposed on shape [48]. For the round glass beads, the coarse beads had the smallest shape and angularity parameters. The relatively larger-shape and angularity parameters for the fine and mixed beads were attributed to the presence of non-rounded particles (Fig. 1). The coarse sand had the largest shape and angularity parameters, whereas the fine sand had the smallest ones. The shape and angularity parameters of the mixed sand followed the ranges of coarse and fine sand. In comparison with the same sieving size range, the angular sand had evidently larger-shape and angularity

parameters than the corresponding round beads. Although the grain morphology obtained from the 2D-SEM is just the projection of grains, the different parameters demonstrated the capability of Fourier representations to distinguish the grain surface morphology.

When analyzing the shape and angularity parameters from the Fourier representations, the selection of the frequency threshold is essential. Wang et al. [48] demonstrated that  $N_1 = 3$  represents a triangular shape,  $N_1 = 4$  represents a square shape, and  $N_1 = 5$  represents multiple corners and simulates the angularity of the grain profiles. The Fourier coefficients of the actual grain profiles are very small when  $N_2 > 25$ ; thus, the corners are very close to each other. In the present study, after several attempts at different grains, we accepted  $N_1 = 5$  as the frequency threshold to distinguish the shape and angularity; that is, the frequency term  $N \leq 4$  was considered to contribute to the shape and  $5 < N \leq 25$  was considered to contribute to the angularity. The grain signature parameters are scale-independent; thus, the same magnification is required when we compare the equivalent diameter, shape and angularity parameters.

**Table 1** Fourier series techniques to characterize the particle morphology of quartz sand and glass bead

| Type        | Sieving size (mm) | Equivalent diameter $d_{eq}$ (mm) | Shape parameter $\alpha_s$ ( $10^{-3} \text{ mm mm}^{-1}$ ) | Angularity parameter $\alpha_r$ ( $10^{-6} \text{ mm mm}^{-1}$ ) |
|-------------|-------------------|-----------------------------------|---|--|
| Glass beads | 0.6–0.9           | $0.74 \pm 0.15$                   | $1.47 \pm 4.87$   | $1.21 \pm 2.39$  |
|             | 1.0–1.4           | $1.33 \pm 0.14$                   | $0.14 \pm 0.49$   | $0.06 \pm 0.03$  |
| Quartz sand | 0.6–1.4           | $1.02 \pm 0.28$                   | $0.65 \pm 1.81$   | $1.55 \pm 4.93$  |
|             | 0.6–0.9           | $1.09 \pm 0.14$                   | $8.52 \pm 5.97$   | $7.59 \pm 6.36$  |
|             | 1.0–1.4           | $1.56 \pm 0.19$                   | $9.20 \pm 7.39$   | $10.02 \pm 20.41$  |
|             | 0.6–1.4           | $1.33 \pm 0.30$                   | $8.50 \pm 5.17$   | $9.02 \pm 11.15$   |



### 3.2 Quantification of the structure using pore-network

The pore networks of the REV's were extracted using the maximal ball algorithm. As the shapes of the real pore cross-sections are complex and highly irregular, idealized shapes are used to approximate them. In the present study, the widely used simple sphere and round cylinder were applied to represent the pore body and throat, respectively. Figure 5 illustrates the networks of the packed glass beads and quartz sand with different sizes. Although a simple shape was used, the extracted networks intuitively demonstrated the differences in the internal pore structures. The fine grains had the highest numbers of pore bodies and throats, whereas the coarse grains had the smallest ones for the same REV size. To quantitatively analyze the difference in the networks, a set of parameters, including pore body radius, pore throat radius, total throat length and coordination number, were calculated (Table 2). The pore body radius mainly varied from 0.05 to 0.30 mm with a mean of 0.168 mm for fine glass beads and it changed from 0.10 to 0.40 mm with a mean of 0.224 mm for the coarse beads. For the angular

quartz sand, the pore body radius mainly varied from 0.09 to 0.32 mm with a mean of 0.177 mm for the fine sand and 0.10–0.42 mm with mean of 0.244 mm for the coarse sand. The mean pore body radius of the mixed grains was between those of the fine and coarse grains. The pore body radius linearly increased with the equivalent grain diameter (Fig. 6), which is consistent with previous experimental and modeling studies [9, 60]. The distribution of the pore body radius followed the lognormal distribution for both glass beads and quartz sand, but with different frequencies (Fig. 7a, e). The mean pore body radius of the angular sand was larger than that of the corresponding round beads with the same sieving size.

The pore throat affected the fluid flow and capillary displacement processes in porous media, as it constrained the conductance and retention. Panels B and F in Fig. 7 depict the pore-throat radius distributions, and panels C and G depict the total throat length distributions for the glass beads and quartz sand, respectively. The distributions of the pore-throat radius and total throat length followed a lognormal distribution as well. However, the mean and frequency varied with the grain morphology. The pore-throat radius

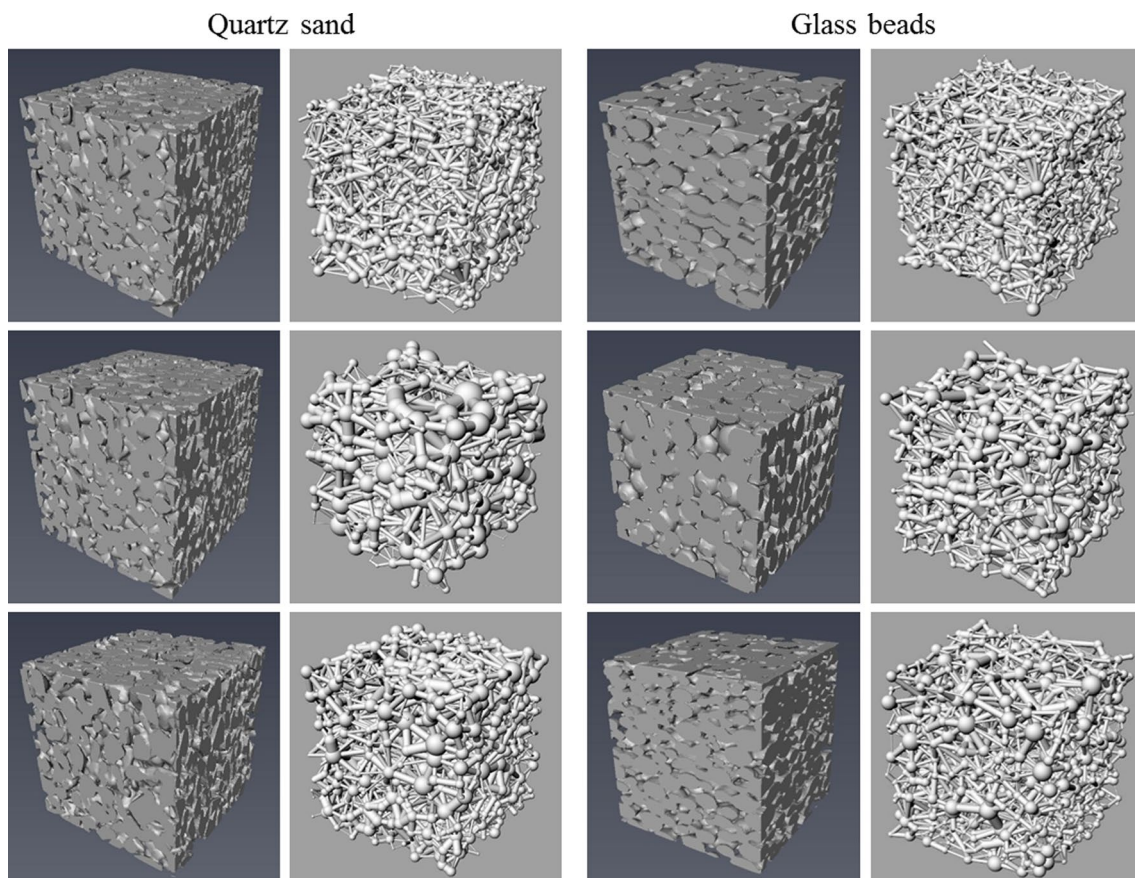


**Fig. 5** Pore structures of 3D REV's and extracted pore-networks using maximal ball algorithm: (Up) 0.6–0.9 mm, (Middle) 1.0–1.4 mm, and (Bottom) 0.6–1.4 mm

**Table 2** Statistics of the parameters to quantify the internal pore network for porous media with different grain sizes and angularities

| Type        | Sieving size (mm) | Number of throats | Number of pores | Pore surface density (mm <sup>-2</sup> mm <sup>-3</sup> ) | Porosity    | Coordination number | Pore radius (mm) | Throat radius (mm) | Total throat length × 10 <sup>3</sup> (mm) |
|-------------|-------------------|-------------------|-----------------|---|-------------|---------------------|------------------|--------------------|--|
| Glass beads | 0.6–0.9           | 7931 ± 868        | 1731 ± 217      | 3.69 ± 0.04   | 0.44 ± 0.01 | 9.0 ± 0.2           | 0.168 ± 0.009    | 0.074 ± 0.003      | 10.04 ± 0.67                               |
|             | 1.0–1.4           | 2662 ± 228        | 707 ± 71        | 2.44 ± 0.03   | 0.39 ± 0.01 | 7.3 ± 0.1           | 0.224 ± 0.009    | 0.105 ± 0.005      | 4.18 ± 0.21                                |
|             | 0.6–1.4           | 4187 ± 1096       | 1251 ± 253      | 2.97 ± 0.19   | 0.35 ± 0.01 | 7.6 ± 0.1           | 0.173 ± 0.017    | 0.075 ± 0.008      | 6.33 ± 0.97                                |
| Quartz sand | 0.6–0.9           | 6736 ± 1266       | 1461 ± 323      | 3.72 ± 0.11   | 0.47 ± 0.03 | 9.1 ± 0.3           | 0.177 ± 0.055    | 0.078 ± 0.007      | 9.24 ± 0.85                                |
|             | 1.0–1.4           | 2325 ± 338        | 551 ± 92        | 2.66 ± 0.08   | 0.45 ± 0.02 | 8.2 ± 0.2           | 0.244 ± 0.014    | 0.107 ± 0.006      | 4.37 ± 0.27                                |
|             | 0.6–1.4           | 4368 ± 841        | 901 ± 208       | 3.22 ± 0.11   | 0.40 ± 0.02 | 8.0 ± 0.2           | 0.179 ± 0.013    | 0.078 ± 0.006      | 7.06 ± 0.64                                |

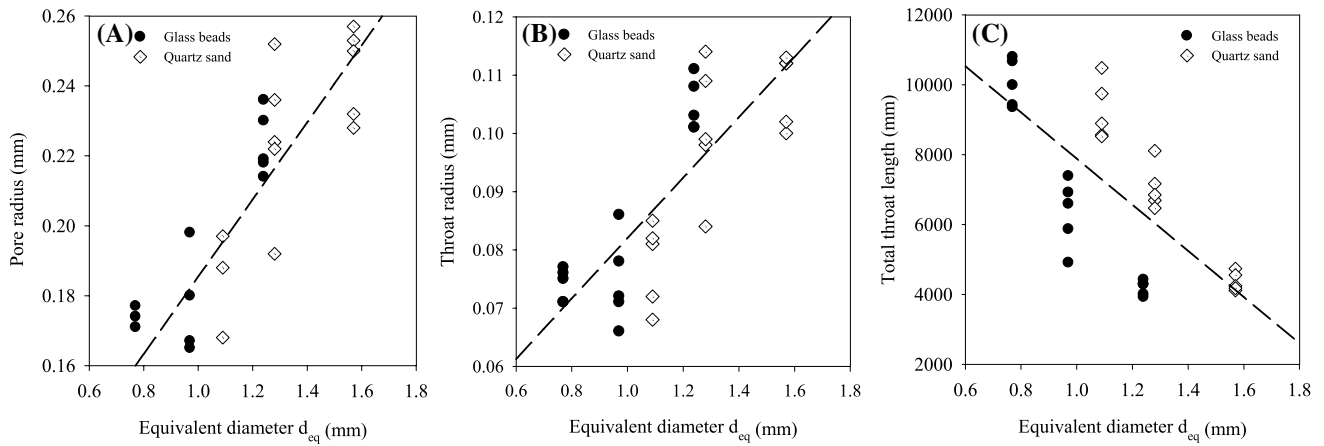


**Fig. 6** Relation between the equivalent diameter and pore-network parameters for glass beads and quartz sand: **a** pore-radius, **b** throat-radius, and **c** total throat length

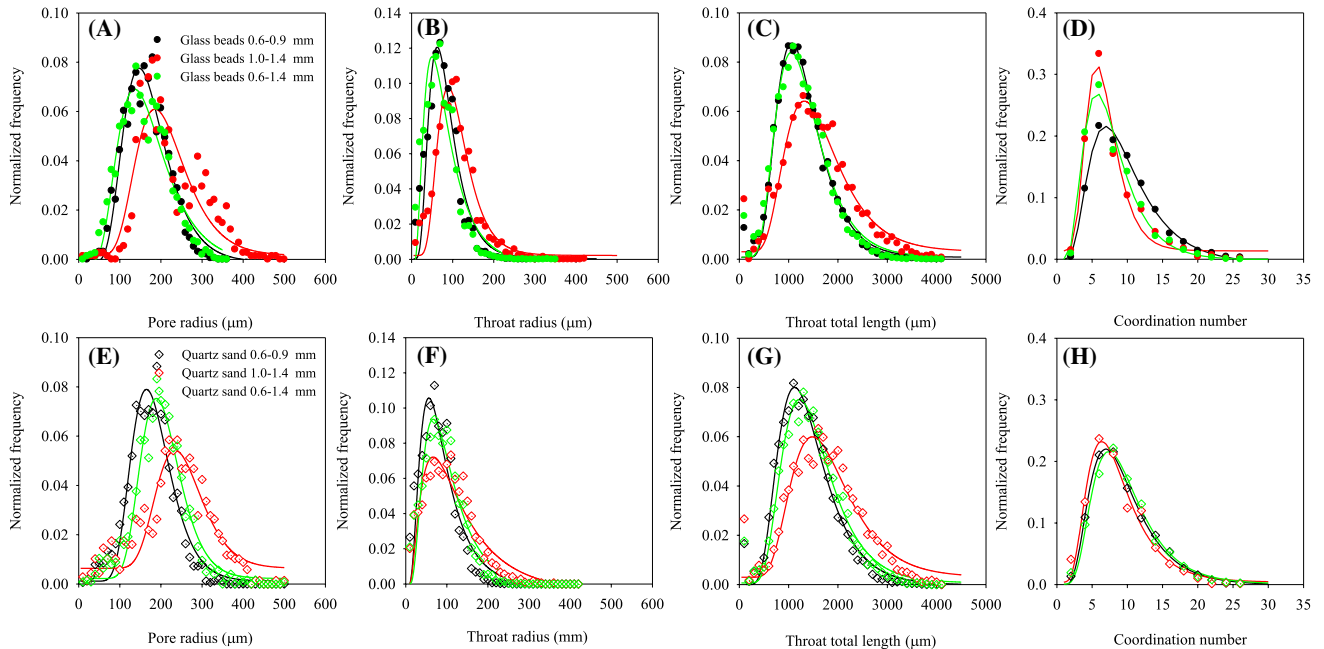


**Fig. 7** Distribution of pore-network parameters for glass beads and quartz sand: **a, e** pore-radius, **b and f** throat-radius, **c and g** total throat length, and **d and h** coordination number

increased with the grain size. The mean pore throat radius of angular quartz sand was slightly larger than that of the corresponding round beads. The total throat length decreased with increasing grain size for an identical REV size. The mean radius of the pore throat was approximately 0.43–0.47 times that of the pore bodies for the angular sand and round beads. This range is consistent with the findings of Ren and Santamarina [61], who clarified that the radius of pore throat is approximately half that of the body.

The coordination number characterizes the connectivity and topology of the pore network. The mean coordination number varied in the range of 7–9. The coarse grain media had a smaller mean coordination number than the fine grain media and the mean coordination number of the mixed grains was between that of the fine and coarse grains. The mean coordination number of angular sand was slightly larger than that of the corresponding round glass beads. The distribution of coordination numbers also followed a lognormal distribution for the glass beads and quartz sand. However, the frequency varied with different grain morphologies (Fig. 7d, h). The lognormal distribution feature is consistent with many other randomly and artificially packed grain particles and natural porous media [62].

### 3.3 Flow and transport properties

#### 3.3.1 Intrinsic permeability

The pore network not only characterizes the internal structure itself but can also be used to estimate the flow and transport parameters with effective computation. Intrinsic permeability is one of the most important characteristics of porous media, which affects the flow and transport behaviors. The intrinsic permeability of different porous media was estimated based on the extracted networks. Table 3 presents the intrinsic permeability in the vertical (Z-direction) and horizontal directions (X-and Y-directions in Cartesian coordinates). The intrinsic permeability in the horizontal direction was 1.2–1.4 times that in the vertical direction for both round beads and angular sand. However, the difference between the two horizontal directions was not distinct. The variation in permeability with direction indicated anisotropic compaction features during the packing processes. The compaction subsequent to the pouring of sand or glass beads may result in different grain orientations and settling in the vertical and horizontal directions [63]. This anisotropic feature is similar to most natural depositions in the soil and aquifer [64, 65].

The intrinsic permeability of fine grains was lower than that of coarse grains for both glass beads and quartz sand. The lowest intrinsic permeability in each direction was obtained for the mixed grains, which had a wider particle size distribution. When comparing columns packed with the

**Table 3** Geometrical tortuosity ( $\tau$ ), intrinsic permeability ( $k$ ) and coefficient of longitudinal dispersivity ( $\alpha_L$ ) of porous media repacked with different grain morphologies in the vertical (Z) and horizontal (X and Y) directions

| Type        | Sieving size (mm) | $\tau$ (-)  |             |             | $k$ ( $\mu\text{m}^2$ ) |           |           | $\alpha_L \times 10^{-3}$ (m) |             |             |
|-------------|-------------------|-------------|-------------|-------------|-------------------------|-----------|-----------|-------------------------------|-------------|-------------|
|             |                   | X           | Y           | Z           | X                       | Y         | Z         | X                             | Y           | Z           |
| Glass beads | 0.6–0.9           | 1.31 ± 0.03 | 1.31 ± 0.04 | 1.65 ± 0.11 | 297 ± 48                | 283 ± 49  | 237 ± 40  | 3.87 ± 0.58                   | 4.32 ± 0.54 | 1.10 ± 0.11 |
|             | 1.0–1.4           | 1.38 ± 0.05 | 1.34 ± 0.05 | 1.83 ± 0.17 | 505 ± 77                | 485 ± 80  | 396 ± 72  | 5.20 ± 2.07                   | 5.46 ± 1.50 | 1.45 ± 0.13 |
|             | 0.6–1.4           | 1.37 ± 0.03 | 1.37 ± 0.03 | 2.01 ± 0.07 | 273 ± 96                | 243 ± 70  | 188 ± 77  | 3.92 ± 0.93                   | 3.49 ± 0.50 | 1.24 ± 0.15 |
| Quartz sand | 0.6–0.9           | 1.31 ± 0.07 | 1.31 ± 0.06 | 1.43 ± 0.07 | 398 ± 150               | 378 ± 140 | 343 ± 131 | 3.73 ± 1.52                   | 4.29 ± 0.62 | 1.13 ± 0.98 |
|             | 1.0–1.4           | 1.32 ± 0.06 | 1.31 ± 0.04 | 1.59 ± 0.23 | 868 ± 173               | 852 ± 227 | 710 ± 203 | 6.93 ± 1.28                   | 6.63 ± 1.03 | 1.62 ± 0.16 |
|             | 0.6–1.4           | 1.25 ± 0.04 | 1.28 ± 0.05 | 1.50 ± 0.14 | 310 ± 103               | 294 ± 101 | 241 ± 98  | 3.71 ± 0.81                   | 4.47 ± 0.75 | 1.24 ± 0.18 |

same sieving size, the intrinsic permeability of the angular sand was 1.1–1.8 times that of the round beads in each direction (Table 3). Intrinsic permeability was in a power-law relation with the means of pore body and throat radii for packed grains with different morphologies (Fig. 8). These power-law relations are consistent with the findings of Gharedaghloo et al. [64] who tested peat soils at different depths. The intrinsic permeability of the coarse grain was more sensitive to the pore and throat radii than that of the fine sand. This can be partly attributed to the larger pores for coarse grains enhancing the hydraulic conductivity [66], and confirms that permeability is most strongly affected by larger pores [9].

The established functional relations between intrinsic permeability and pore structure include the Kozeny–Carman

equation or the power laws of porosity [67, 68]. The fitting of intrinsic permeability versus porosity for the different angular sand and round beads indicated that the porous media with the same sieving size followed the power-law curve (Fig. 9a, b). In addition, the coefficients of the power-law equation differed from the flow direction owing to the anisotropic feature. The power-law equation had different coefficients for the different sieving size groups. The different fitting curves for grains with different sizes and distributions indicate that the grain size, distribution, and shape are critical factors for intrinsic permeability. Liu and Jeng [69] demonstrated that porosity, particle size, particle surface, and particle shape have different influence intensities on intrinsic permeability. They clarified that porosity is the most sensitive impact factor, followed by particle size. In

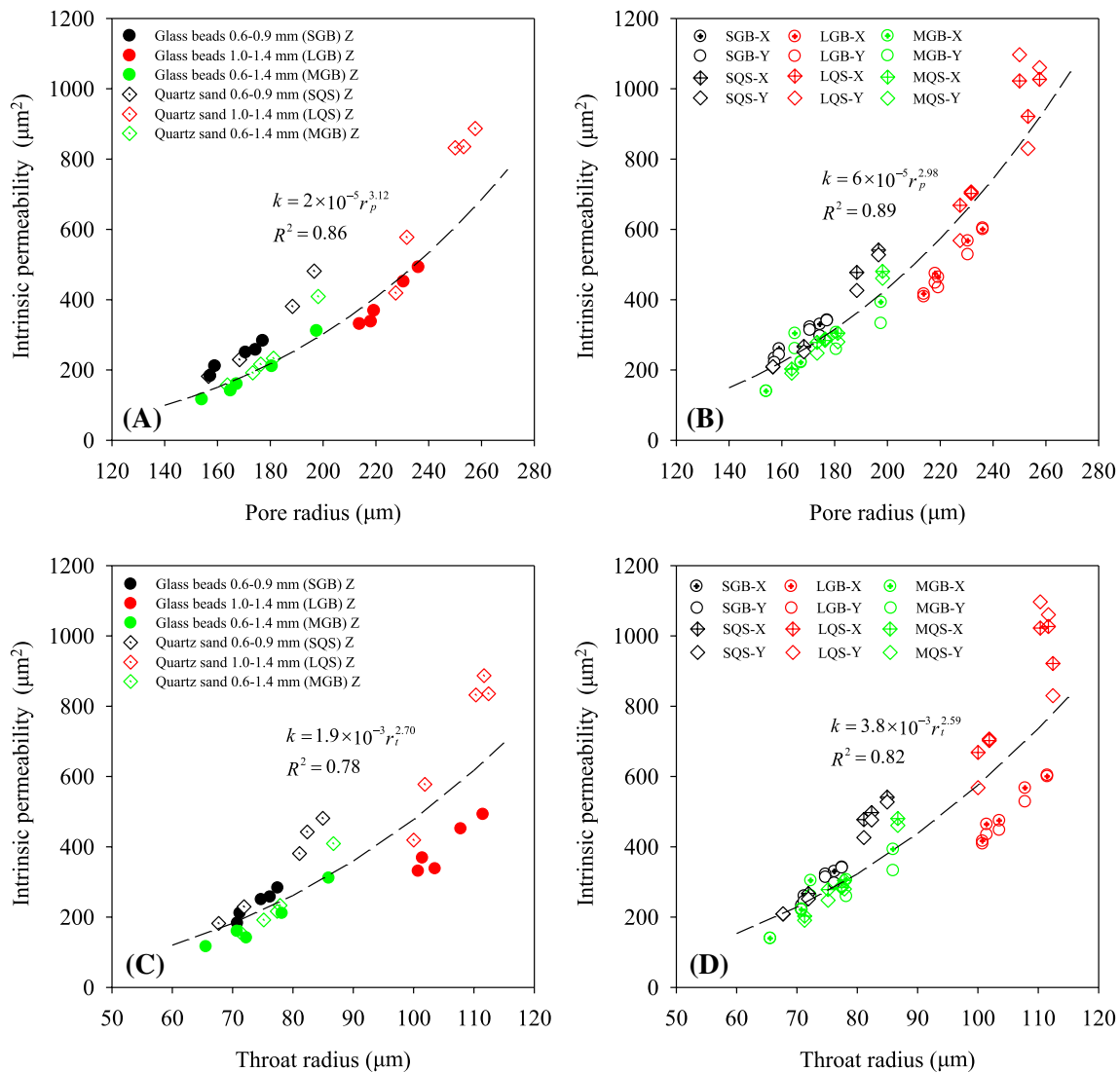


**Fig. 8** Effect of pore network parameters on intrinsic permeability in different directions for glass beads and quartz sand: **a, b** pore-radius, and **c, d** throat-radius in vertical and horizontal direction, respectively

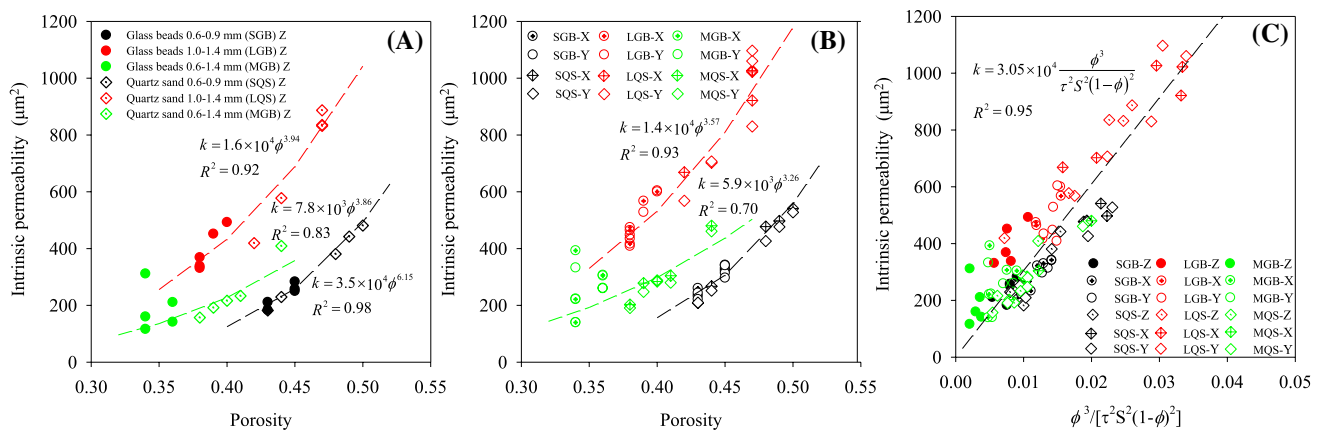


**Fig. 9** Diverse parameters correlate to the intrinsic permeability of porous media: **a, b** the relationship between intrinsic permeability and porosity in vertical and horizontal direction, respectively and **c** the Kozeny–Carman relation in vertical and horizontal direction

general, the relations between the intrinsic permeability and porosity of the packed round beads and angular sand are consistent with those of other artificially packed grains [9].

In the power-law equation, intrinsic permeability is only related to porosity, whereas the other pore characteristics (such as tortuosity and pore interface area) are lumped in the coefficients. As mentioned above, this simplification results in different fitting coefficients in the vertical and horizontal directions [67, 69]. The Kozeny–Carman equation, considering the tortuosity and pore surface of the pore system, is expressed as [70]

$$k = \lambda \frac{\phi^3}{\tau^2 S^2 (1 - \phi)^2} \tag{18}$$

where  $\lambda$  is a generalized factor accounting for different pore shapes,  $S$  is the specific surface area of the pores, and  $\tau$  is the geometric tortuosity, which is defined as the ratio of the average length of the true path that molecules travel through a porous medium to the length of the straight line across the porous media. As shown in Fig. 9c, a single linear curve fits the relation between intrinsic permeability and  $\phi^3 / [\tau^2 S^2 (1 - \phi)^2]$  for porous media with different grain sizes and angularities. Although intrinsic permeability varies with direction, the Kozeny–Carman equation also performs well for anisotropic features. This indicates the robustness of this equation, and thus, it can be used to mimic intrinsic permeability and serve as a quality-control tool for porous media with different grain morphologies.

### 3.3.2 Water–retention curves

Primary drainage curves were obtained through pore-network simulations conducted for diverse porous media. Figure 10 illustrates the primary drainage curves obtained for the sampled REV's, and the fitting parameters of the van

Genuchten model are presented in Table 4. The coefficients of determination of all fitting curves exceeded 0.97, which demonstrated a good agreement with the results obtained using the van Genuchten model. The fitted  $\theta_s$  values were consistent with the porosity of the packed porous media (Table 2). The parameters  $\alpha$  and  $n$  are measures of the pore-size distribution [71, 72]. The highest value of  $\alpha$  was obtained in columns packed with coarse particle sizes for both glass beads and quartz sand. The parameter  $\alpha$  of the mixed samples was between the coarse and fine grains. Its value increased with the pore radius and throat radius, which have a controlling effect on the entry pressure of pores [9]. The parameter  $n$  is generally used to characterize the pore size distribution. In the present study, the pore size distribution was in a relatively narrow range owing to the small range of grain distribution (0.6–1.4 mm); thus, the variation of parameter  $n$  was not clear for both round glass beads and angular quartz sand. This result is consistent with those obtained by several previous studies [9, 73, 74].

### 3.3.3 Hydrodynamic dispersion

Pore-scale heterogeneities are present in all porous media, leading to deviations from the mean flow. This is described by the hydrodynamic dispersion on a macroscale. The breakthrough curve of a solute may perform like Fickian or non-Fickian behavior [75]. Solute transport in the REV's of round beads and angular sand exhibited Fickian behavior (Fig. 4). Similar phenomena were observed by Meyer and Bijeljic [76], who found that the transport behavior converges from an initial ballistic dispersion to Fickian diffusion in the longitudinal direction. Whether solute transport appears in Fickian or non-Fickian form is dependent on several factors, such as fluid velocity (Peclet number), tortuosity, and pore connectivity. Based on the numerical simulation of lattice network, Vasilyev et al. [77] found that anomalous transport

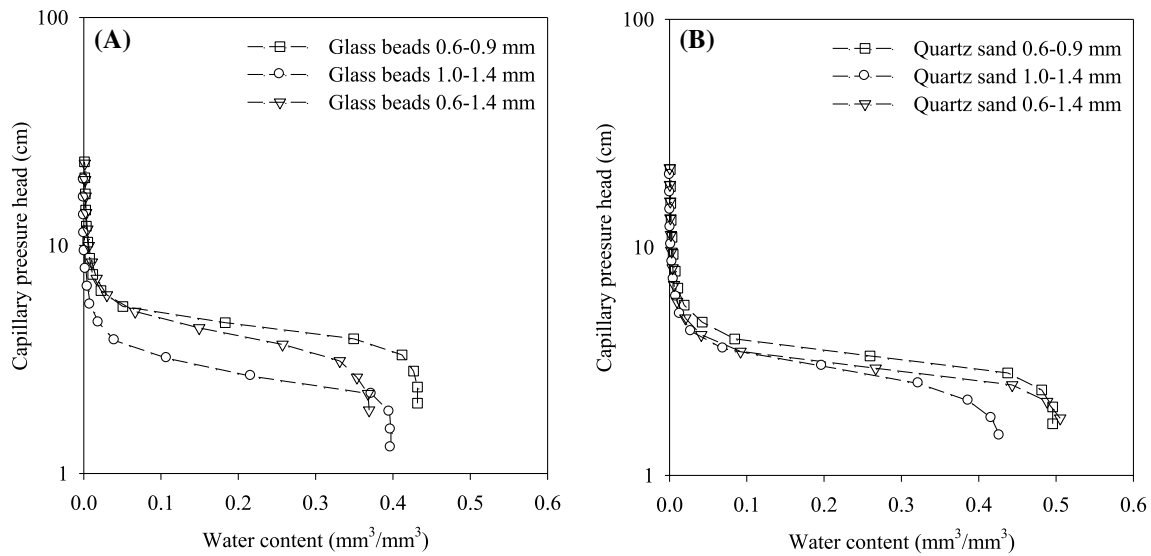


**Fig. 10** Primary drainage curves for porous media with different angularities: **a** glass beads and **b** quartz sand

**Table 4** Fitting parameters of van Genuchten model for water retention curve of different porous media

| Particle type | Particle size (mm) | van Genuchten parameters |                             |       | $R^2$ |
|---------------|--------------------|--------------------------|-----------------------------|-------|-------|
|               |                    | $\theta_s$               | $\alpha$ (m <sup>-1</sup> ) | $n$   |       |
| Glass beads   | 0.6–0.9            | 0.45                     | 24.20                       | 10.69 | 0.99  |
|               | 1.0–1.4            | 0.39                     | 34.23                       | 8.13  | 0.99  |
|               | 0.6–1.4            | 0.35                     | 26.35                       | 7.15  | 0.97  |
| Quartz sand   | 0.6–0.9            | 0.47                     | 26.95                       | 9.83  | 0.98  |
|               | 1.0–1.4            | 0.46                     | 39.57                       | 8.18  | 0.98  |
|               | 0.6–1.4            | 0.41                     | 34.62                       | 9.82  | 0.98  |

in the form of long tails of concentration curves appeared when the coordination number exceeded 6. However, the mean coordination number varied in the range of 7–9 for both round beads and angular sand, which was slightly larger than the critical value of 6. The breakthrough curve did not exhibit an anomalous appearance, early arrival, or long-tailing features. This is attributable to the coordination number distribution, geometrical tortuosity, and selection of a simple geometrical shape (spherical or round cylindrical) to represent the pore network. Wang and Bayani Cardenas [75] demonstrated that longitudinal transport can also transit from non-Fickian to Fickian form at incrementally increasing scales.

Hydrodynamic dispersion refers to the stretching of a solute plume in the flow direction during transport with fluid flow. The dispersion along the flow direction is called longitudinal dispersion, whereas that perpendicular to the flow is called transversal dispersion. Table 3 shows the coefficients of longitudinal dispersivity ( $\alpha_L$ ) in different directions for

different quartz sand and glass beads. The largest  $\alpha_L$  value was obtained from the coarse glass beads and quartz sand, whereas the fine glass beads and quartz sand had the lowest values. The  $\alpha_L$  value for the mixed grains ranged between that of the coarse and fine grains. The value of  $\alpha_L$  did not distinctly differ between angular sand and round beads for the same sieving size (Table 3). The value  $\alpha_L$  increased with a larger grain size distribution, which agrees with the result obtained by Klotz et al. [78], who tested soil samples and observed that the dispersivity increased with the particle diameter. The value of  $\alpha_L$  in the horizontal direction was approximately 3–4 times that in the vertical direction for different sand and beads. However, the value of  $\alpha_L$  in the two horizontal directions did not evidently differ in each REV. This anisotropic feature is consistent with that of permeability.

The coordination number characterizes the connectivity of pores in the porous media, which influences the complicated flow path and solute transport. The tortuosity decreases with an increase in the mean coordination number (Tables 2 and 3), which means that the flow paths become similar to a straight line in the flow direction, and the mean value together with variations in velocity, decrease as the coordination number increases [77]. This leads to a smaller variance in the velocities of all paths. The coefficient of longitudinal dispersivity decreased with an increase in the coordination number (Fig. 11). Vasilyev et al. [77] proposed an empirical formula to quantify the coefficient of dispersivity induced by the internal pore structure (geometric dispersivity coefficient),  $\alpha_L = \alpha_0 + c \cdot e^{-\psi(C_n^{-2})}$ , where  $\alpha_0$  is the geometric dispersivity at the highest mean network coordination number ( $C_n = 26$ ),  $c$  and  $\delta$  are constants, and  $C_n$  is the mean network coordination number. This formula

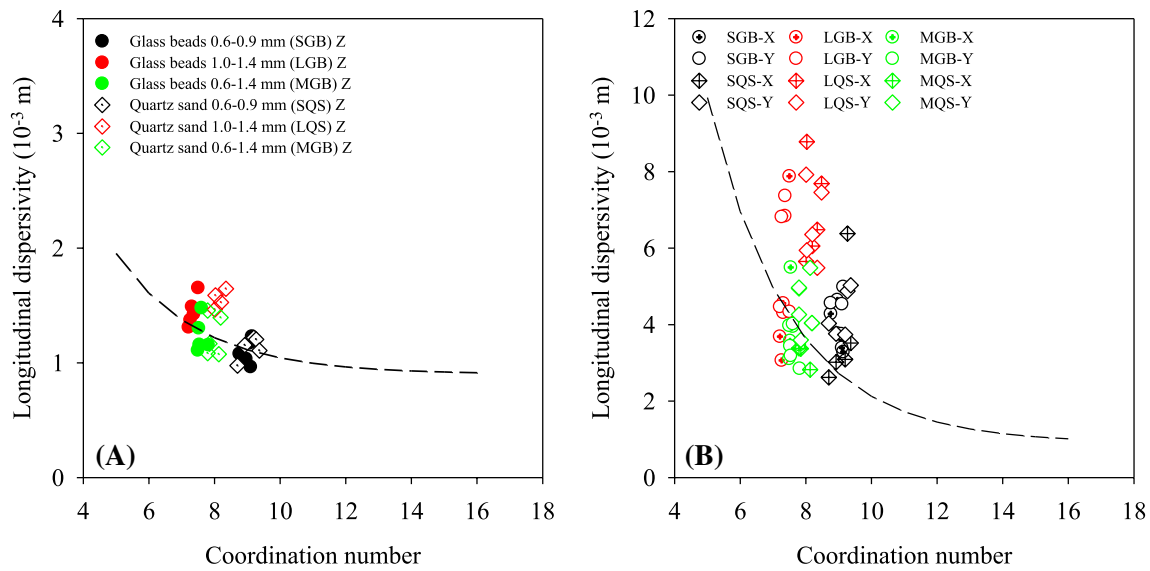


**Fig. 11** Effect of coordination number on longitudinal dispersivity in different directions for glass beads and quartz sand: **a** vertical direction and **b** horizontal direction

works sufficiently well for  $C_n \geq 4$ . Even though the mean coordination numbers for the packing glass beads and quartz sand in the present study fell in the range of 79, which is relatively narrow, the fitting results suggested the agreement of this formula for random pore networks, particularly in the vertical direction (Fig. 11).

### 4 Conclusions

This study aims to investigate the effect of grain morphology on the internal pore structure, as well as the flow and transport properties, of unconsolidated porous media. Different pore structures were generated by the random packing of grains with different morphologies. A small grain size range was arbitrarily selected to minimize the influence of grain non-uniformity. The grain morphology was obtained through SEM and analyzed using Fourier analysis. Pore networks were extracted from 3D CT images.

The results of a Fourier analysis indicated that the obtained equivalent sizes of the round beads were close to the mean values of the sieving size, whereas those of angular sand were slightly larger than the corresponding mean sieving sizes. The angular sand had evidently larger shape and angularity parameters than the corresponding round beads. Moreover, the results demonstrated the capability of the shape and angularity parameters to distinguish the grain-surface morphology.

The extracted pore networks distinguished the effects of grain morphology on pore structure. The means of the pore-body radius, pore-throat radius, and coordination number linearly increased with the equivalent grain diameter. The

means of pore-body radius, pore-throat radius, and coordination number of the angular sand were larger than those of the corresponding round beads with the same sieving size. The distributions of pore-body radius, pore-throat radius, total throat length, and coordination number followed lognormal distribution.

The estimated intrinsic permeability exhibited anisotropic features in packed round sand and angular beads. The intrinsic permeability in the horizontal direction was 1.2–1.4 times that in the vertical direction. In addition, for both glass beads and quartz sand, the intrinsic permeability of fine grains was lower than that of coarse grains. The lowest intrinsic permeability in each direction was obtained for mixed grains. A comparison of the columns packed with the same sieving size, the intrinsic permeability of the angular sand was evidently larger than that of the round beads in each direction. The relation between intrinsic permeability and porosity followed the Kozeny–Carman equation for both round beads and angular sand.

Fickian transport behaviors were detected in the REV's of both angular sand and round beads. The coefficient of longitudinal dispersivity in the vertical direction was approximately 3–4 times that in the horizontal direction owing to the anisotropic compaction of grains. The coefficient of longitudinal dispersivity decreased with an increase in the grain size. In general, the difference in the longitudinal dispersivity coefficient was not distinct between the angular sand and round beads for the same sieving size. The longitudinal dispersivity decreased with an increase in the coordination number regardless of grain morphology.

The findings of this study help us better understand the effects of grain morphology on the pore structure and

macroscopic flow and transport properties, such as permeability and hydrodynamic dispersion. This provides a reference for the research and application of diverse engineering techniques, such as exploration of oil, storage and sequestration of CO<sub>2</sub>, remediation of contaminants in the aquifer, and industrial drying and filtration techniques.

**Acknowledgements** This research is partially supported by National Natural Science Foundation of China (Grant nos. 51879264, 51790535). The authors are grateful to Dr. Martin J. Blunt for providing the pore-network extraction code. We also thank Dr. Alex Furman for his critical comments.

## Declarations

**Conflict of interest** No conflict of interest.

## References

- Al-Raoush, R.I.: Experimental investigation of the influence of grain geometry on residual NAPL using synchrotron microtomography. *J. Contam. Hydrol.* **159**, 1–10 (2014)
- Chaudhary, K., Cardenas, M.B., Wolfe, W.W., Maisano, J.A., Ketcham, R.A., Bennett, P.C.: Pore-scale trapping of supercritical CO<sub>2</sub> and the role of grain wettability and shape. *Geophys. Res. Lett.* **40**(15), 3878–3882 (2013)
- Lee, B.Y., Kurtis, K.E.: Effect of pore structure on salt crystallization damage of cement-based materials: consideration of w/b and nanoparticle use. *Cem. Concr. Res.* **98**, 61–70 (2017)
- Caplan, J.S., Gimenez, D., Subroy, V., Heck, R.J., Prior, S.A., Runion, G.B., Torbert, H.A.: Nitrogen-mediated effects of elevated CO<sub>2</sub> on intra-aggregate soil pore structure. *Glob. Change. Biol.* **23**(4), 1585–1597 (2017)
- Palombo, M., Gabrielli, A., Servedio, V.D.P., Ruocco, G., Capuani, S.: Structural disorder and anomalous diffusion in random packing of spheres. *Sci. Rep.* (2013). <https://doi.org/10.1038/srep02631>
- Vanson, J.M., Boutin, A., Klotz, M., Coudert, F.X.: Transport and adsorption under liquid flow: the role of pore geometry. *Soft Matter* **13**(4), 875–885 (2017)
- Geistlinger, H., Ataei-Dadavi, I., Mohammadian, S., Vogel, H.J.: The impact of pore structure and surface roughness on capillary trapping for 2-D and 3-D porous media: comparison with percolation theory. *Water. Resour. Res.* **51**(11), 9094–9111 (2015)
- Lin, C.L., Miller, J.D.: Pore structure analysis of particle beds for fluid transport simulation during filtration. *Int. J. Miner. Process.* **73**(2–4), 281–294 (2004)
- Mahmoodlu, M.G., Raoof, A., Sweijen, T., van Genuchten, M.T.: Effects of Sand Compaction and Mixing on Pore Structure and the Unsaturated Soil Hydraulic Properties. *Vadose Zone J.* **15**(8), 0 (2016)
- Mecke, K., Arns, C.H.: Fluids in porous media: a morphometric approach. *J. Phys-Condens. Mat.* **17**(9), S503–S534 (2005)
- Niya, S.M.R., Selvadurai, A.P.S.: The estimation of permeability of a porous medium with a generalized pore structure by geometry identification. *Phys. Fluids.* **29**(3), 037101 (2017)
- Rad, M.N., Shokri, N.: Effects of grain angularity on NaCl precipitation in porous media during evaporation. *Water. Resour. Res.* **50**(11), 9020–9030 (2014)
- Narsilio, G.A., Buzzi, O., Fityus, S., Yun, T.S., Smith, D.W.: Upscaling of Navier-Stokes equations in porous media: theoretical, numerical and experimental approach. *Comput. Geotech.* **36**(7), 1200–1206 (2009)
- Torskaya, T., Shabro, V., Torres-Verdin, C., Salazar-Tio, R., Revil, A.: Grain shape effects on permeability, formation factor, and capillary pressure from pore-scale modeling. *Transp. Porous. Med.* **102**(1), 71–90 (2014)
- Metzger, T., Irawan, A., Tsotsas, E.: Influence of pore structure on drying kinetics: a pore network study. *AIChE J.* **53**(12), 3029–3041 (2007)
- Horgan, G.W., Ball, B.C.: Simulating Diffusion in a Boolean Model of Soil Pores. *Eur. J. Soil. Sci.* **45**(4), 483–491 (1994)
- Bijeljic, B., Mostaghimi, P., Blunt, M.J.: Insights into non-Fickian solute transport in carbonates. *Water. Resour. Res.* **49**(5), 2714–2728 (2013)
- Bijeljic, B., Raeini, A., Mostaghimi, P., Blunt, M.J.: Predictions of non-Fickian solute transport in different classes of porous media using direct simulation on pore-scale images. *Phys. Rev. E* (2013). <https://doi.org/10.1103/PhysRevE.87.013011>
- Zhokh, A., Strizhak, P.: Crossover between Fickian and non-Fickian diffusion in a system with hierarchy. *Microporous Mesoporous Mater.* **282**, 22–28 (2019)
- Zhang, C.Y., Werth, C.J., Webb, A.G.: A magnetic resonance imaging study of dense nonaqueous phase liquid dissolution from angular porous media. *Environ. Sci. Technol.* **36**(15), 3310–3317 (2002)
- Gácsi, Z., Kovács, J., Pieczonka, T.: Particle arrangement characterization by the pair correlation function. *Powder Metall. Prog.* **3**(1), 30 (2003)
- Cho, G.C., Dodds, J., Santamarina, J.C.: Particle shape effects on packing density, stiffness, and strength: natural and crushed sands. *J. Geotech. Geoenviron.* **132**(5), 591–602 (2006)
- Katagiri, J., Matsushima, T., Yamada, Y., Tsuchiyama, A., Nakano, T., Uesugi, K., Ohtake, M., Saiki, K.: Investigation of 3D grain shape characteristics of lunar soil retrieved in apollo 16 using image-based discrete-element modeling. *J. Aerospace. Eng.* **28**(4), 04014092 (2015)
- Bowman, E.T., Soga, K., Drummond, W.: Particle shape characterisation using Fourier descriptor analysis. *Geotechnique* **51**(6), 545–554 (2001)
- Laubie, H., Radjai, F., Pellenq, R., Ulm, F.J.: Stress transmission and failure in disordered porous media. *Phys. Rev. Lett.* (2017). <https://doi.org/10.1103/PhysRevLett.119.075501>
- Wang, Z.Z., Chauhan, K., Pereira, J.M., Gan, Y.X.: Disorder characterization of porous media and its effect on fluid displacement. *Phys. Rev. Fluids* (2019). <https://doi.org/10.1103/PhysRevFluids.4.034305>
- Bultreys, T., Boone, M.A., Boone, M.N., De Schryver, T., Masschaele, B., Van Hoorebeke, L., Cnudde, V.: Fast laboratory-based micro-computed tomography for pore-scale research: illustrative experiments and perspectives on the future. *Adv. Water. Resour.* **95**, 341–351 (2016)
- Hertel, S., Hunter, M., Galvosas, P.: Magnetic resonance pore imaging, a tool for porous media research. *Phys. Rev. E.* (2013). <https://doi.org/10.1103/PhysRevE.87.030802>
- Wildenschild, D., Sheppard, A.P.: X-ray imaging and analysis techniques for quantifying pore-scale structure and processes in subsurface porous medium systems. *Adv. Water. Resour.* **51**, 217–246 (2013)
- Iassonov, P., Gebrenegus, T., Tuller, M.: Segmentation of X-ray computed tomography images of porous materials: a crucial step for characterization and quantitative analysis of pore structures. *Water Resour. Res.* (2009). <https://doi.org/10.1029/2009WR008087>



31. Kaestner, A., Lehmann, E., Stampanoni, M.: Imaging and image processing in porous media research. *Adv. Water. Resour.* **31**(9), 1174–1187 (2008)
32. Anovitz, L.M., Cole, D.R.: Characterization and analysis of porosity and pore structures. *Rev. Mineral Geochem.* **80**, 61–164 (2015)
33. Arns, C.H., Knackstedt, M.A., Mecke, K.R.: Characterising the morphology of disordered materials. *Lect Notes Phys.* **600**, 37–74 (2002)
34. Young, I.M., Crawford, J.W., Rappoldt, C.: New methods and models for characterising structural heterogeneity of soil. *Soil. Till. Res.* **61**(1–2), 33–45 (2001)
35. Cardenas, J.P., Santiago, A., Tarquis, A.M., Losada, J.C., Borondo, F., Benito, R.M.: Soil porous system as heterogeneous complex network. *Geoderma* **160**(1), 13–21 (2010)
36. Hunt, A.G., Ewing, R.P., Horton, R.: What's wrong with soil physics? *Soil. Sci. Soc. Am. J.* **77**(6), 1877–1887 (2013)
37. Al-Kharusi, A.S., Blunt, M.J.: Network extraction from sandstone and carbonate pore space images. *J. Petrol. Sci. Eng.* **56**(4), 219–231 (2007)
38. Blunt, M.J., Bijeljic, B., Dong, H., Gharbi, O., Iglauer, S., Mostaghimi, P., Paluszny, A., Pentland, C.: Pore-scale imaging and modelling. *Adv. Water Resour.* **51**, 197–216 (2013)
39. Dashtian, H., Shokri, N., Sahimi, M.: Pore-network model of evaporation-induced salt precipitation in porous media: the effect of correlations and heterogeneity. *Adv. Water Resour.* **112**, 59–71 (2018)
40. Ovaysi, S., Piri, M.: Direct pore-level modeling of incompressible fluid flow in porous media. *J. Comput. Phys.* **229**(19), 7456–7476 (2010)
41. Tartakovsky, A.M., Meakin, P.: A smoothed particle hydrodynamics model for miscible flow in three-dimensional fractures and the two-dimensional Rayleigh-Taylor instability. *J. Comput. Phys.* **207**(2), 610–624 (2005)
42. Inamuro, T., Ogata, T., Tajima, S., Konishi, N.: A lattice Boltzmann method for incompressible two-phase flows with large density differences. *J. Comput. Phys.* **198**(2), 628–644 (2004)
43. Fourie, W., Said, R., Young, P. and Barnes, D.: The simulation of pore scale fluid flow with real world geometries obtained from X-ray computed tomography. In *Proceedings of the COMSOL Conference, Boston* (2007)
44. Aghaei, A., Piri, M.: Direct pore-to-core up-scaling of displacement processes: Dynamic pore network modeling and experimentation. *J. Hydrol.* **522**, 488–509 (2015)
45. Jivkov, A.P., Hollis, C., Etiese, F., McDonald, S.A., Withers, P.J.: A novel architecture for pore network modelling with applications to permeability of porous media. *J. Hydrol.* **486**, 246–258 (2013)
46. Mahmoodlu, M.G., Raouf, A., Bultreys, T., Van Stappen, J., Cnudde, V.: Large-scale pore network and continuum simulations of solute longitudinal dispersivity of a saturated sand column. *Adv. Water Resour.* **144**, 103713 (2020)
47. Rabbani, H.S., Seers, T.D., Guerillot, D.: Analytical pore-network approach (APNA): a novel method for rapid prediction of capillary pressure-saturation relationship in porous media. *Adv. Water. Resour.* **130**, 147 (2019)
48. Wang, L.B., Wang, X.R., Mohammad, L., Abadie, C.: Unified method to quantify aggregate shape angularity and texture using fourier analysis. *J. Mater. Civ. Eng.* **17**(5), 498–504 (2005)
49. Otsu, N.: A threshold selection method from gray-level histograms. *IEEE Trans. Syst. Man Cybern.* **9**(1), 62–66 (1979)
50. Costanza-Robinson, M.S., Estabrook, B.D., Fouhey, D.F.: Representative elementary volume estimation for porosity, moisture saturation, and air-water interfacial areas in unsaturated porous media: data quality implications. *Water Resour. Res.* (2011). <https://doi.org/10.1029/2010WR009655>
51. Fernandes, J.S., Appoloni, C.R., Fernandes, C.P.: Determination of the representative elementary volume for the study of sandstones and siltstones by X-ray microtomography. *Mater. Res. Ibero-Am J.* **15**(4), 662–670 (2012)
52. Xiong, Y., Dai, J., Zhang, X., Huang, G., Furman, A.: Quantitative assessment of the heterogeneity and reproducibility of repacked silica sand columns. *Vadose Zone J.* **16**(13), 1 (2017)
53. Xiong, Y., Long, X., Huang, G., Furman, A.: Impact of pore structure and morphology on flow and transport characteristics in randomly repacked grains with different angularities. *Soils Found.* **59**, 15 (2019)
54. Dong, H., Blunt, M.J.: Pore-network extraction from micro-computerized-tomography images. *Phys Rev.* (2009). <https://doi.org/10.1103/PhysRevE.80.036307>
55. Silin, D., Patzek, T.: Pore space morphology analysis using maximal inscribed spheres. *Phys. Stat. Mech. Appl.* **371**(2), 336–360 (2006)
56. Luo, G., Ji, Y., Wang, C.-Y., Sinha, P.K.: Modeling liquid water transport in gas diffusion layers by topologically equivalent pore network. *Electrochim. Acta* **55**(19), 5332–5341 (2010)
57. Gostick, J., Aghighi, M., Hinebaugh, J., Tranter, T., Hoeh, M.A., Day, H., Spellacy, B., Sharqawy, M.H., Bazylak, A., Burns, A., Lehnert, W., Putz, A.: OpenPNM: a pore network modeling package. *Comput. Sci. Eng.* **18**(4), 60–74 (2016)
58. van Genuchten, M.T.: A closed-form equation for predicting the hydraulic conductivity of unsaturated soils. *Soil. Sci. Soc. Am. J.* **44**(5), 892–898 (1980)
59. Delgado, J.M.P.Q.: Longitudinal and transverse dispersion in porous media. *Chem. Eng. Res. Des.* **85**(9), 1245–1252 (2007)
60. Hamamoto, S., Moldrup, P., Kawamoto, K., Sakaki, T., Nishimura, T., Komatsu, T.: Pore network structure linked by X-ray CT to particle characteristics and transport parameters. *Soils Found.* **56**(4), 676–690 (2016)
61. Ren, X.W., Santamarina, J.C.: The hydraulic conductivity of sediments: A pore size perspective. *Eng. Geol.* **233**, 48–54 (2018)
62. Willson, C.S., Lu, N., Likos, W.J.: Quantification of grain, pore, and fluid microstructure of unsaturated sand from X-ray computed tomography images. *Geotech. Test. J.* **35**(6), 911–923 (2012)
63. Sufian, A., Russell, A.R., Whittle, A.J., Saadatfar, M.: Pore shapes, volume distribution and orientations in monodisperse granular assemblies. *Granul. Matter.* **17**(6), 727–742 (2015)
64. Gharedaghloo, B., Price, J.S., Rezaeezad, F., Quinton, W.L.: Evaluating the hydraulic and transport properties of peat soil using pore network modeling and X-ray micro computed tomography. *J. Hydrol.* **561**, 494–508 (2018)
65. Zhu, J.: Effect of layered structure on anisotropy of unsaturated soils. *Soil Sci.* **177**(2), 139–146 (2012)
66. Assouline, S.: Modeling the relationship between soil bulk density and the water retention curve. *Vadose Zone J.* **5**(2), 554 (2006)
67. Schulz, R., Ray, N., Zech, S., Rupp, A., Knabner, P.: Beyond Kozeny-carman: predicting the permeability in porous media. *Transp. Porous. Med.* **130**(2), 487–512 (2019)
68. Torskaya, T., Shabro, V., Torres-Verdín, C., Salazar-Tio, R., Revil, A.: Grain shape effects on permeability, formation factor, and capillary pressure from pore-scale modeling. *Transp. Porous Media* **102**(1), 71–90 (2013)
69. Liu, Y.F., Jeng, D.S.: Pore scale study of the influence of particle geometry on soil permeability. *Adv. Water Resour.* **129**, 232 (2019)
70. Neithalath, N., Sumanasooriya, M.S., Deo, O.: Characterizing pore volume, sizes, and connectivity in pervious concretes for permeability prediction. *Mater. Charact.* **61**(8), 802–813 (2010)
71. Lenhard, R.J., Parker, J.C., Mishra, S.: On the correspondence between Brooks-Corey and van Genuchten models. *J. Irrig. Drain. Eng.* **115**(4), 610–611 (1989)

72. Van Genuchten, M.T., Nielsen, D.R.: On describing and predicting the hydraulic properties of unsaturated soils. *Ann. Geophys.* **3**(5), 615–628 (1985)
73. Richard, G., Sillon, J.F., Marloie, O.: Comparison of inverse and direct evaporation methods for estimating soil hydraulic properties under different tillage practices. *Soil Sci. Soc. Am. J.* **65**, 215–224 (2001)
74. Stange, C.F., Horn, R.: Modeling the soil water retention curve for conditions of variable porosity. *Vadose Zone J.* **4**(3), 602–613 (2005)
75. Wang, L., Bayani Cardenas, M.: Transition from non-Fickian to Fickian longitudinal transport through 3-D rough fractures: scale-(in)sensitivity and roughness dependence. *J. Contam. Hydrol.* **198**, 1–10 (2017)
76. Meyer, D.W., Bijeljic, B.: Pore-scale dispersion: bridging the gap between microscopic pore structure and the emerging macroscopic transport behavior. *Phys. Rev. E.* (2016). <https://doi.org/10.1103/PhysRevE.94.013107>
77. Vasilyev, L., Raoof, A., Nordbotten, J.M.: Effect of mean network coordination number on dispersivity characteristics. *Transp. Porous. Med.* **95**(2), 447–463 (2012)
78. Klotz, D., Seiler, K.P., Moser, H., Neumaier, F.: Dispersivity and velocity relationship from laboratory and field experiments. *J. Hydrol.* **45**(3), 169–184 (1980)

**Publisher's Note** Springer Nature remains neutral with regard to jurisdictional claims in published maps and institutional affiliations.